Quantifying 3D Modeling Errors in Time-Domain Electromagnetics: Implications for Deterministic and Probabilistic Inversions

Frederik Alexander Falk, Anders Vest Christiansen, and Thomas Mejer Hansen

Department of Geoscience, Aarhus University
Høegh-Guldbergs Gade 2, 8000 Aarhus, Denmark

ABSTRACT

Subsurface resistivity in geophysics is commonly estimated indirectly from dependent measurements. This relationship can be approximated in a forward operator using physical models, such as Maxwell's equations for time-domain electromagnetics (TDEM), where measured voltages in receiver coils arise from decaying magnetic fields. In TDEM, the inverse operator usually does not exist, so inversion methods estimate resistivity by incorporating measurements, prior information, error assumptions, and the forward operator. A common assumption in forward models is that the subsurface is one-dimensional (1D), with resistivity varying only vertically. When lateral variations are present, this assumption introduces a 3D modeling error. Understanding these errors and their resulting artifacts is crucial, as the 1D assumption is widely used but often inaccurate. The effect of 3D modeling errors in TDEM inversion is examined using three distinct three-layer geological model types: a buried valley, a lens at the surface, and variation in topography. Realistic 3D data are computed for each of the three scenarios, and the impact of using deterministic and probabilistic 1D inversion is investigated. In all three cases, features appear in the solution to the inverse problem that are not consistent with the reference model. The erroneous features can be directly linked to using a 1D forward model to describe 3D data. Goodness-of-fit metrics such as the normalized data residual are analyzed and found to be unreliable indicators of whether the inversion model structure is real or a 3D artifact. Lastly, a case is presented where inversion models of SkyTEM data from Ribe in southern Denmark show structures similar to those found in the analysis, highlighting the applicability of this analysis to interpretations of real TDEM datasets.

INTRODUCTION

The time-domain electromagnetic (TDEM) method is widely used in exploration geophysics due to its ability to non-invasively obtain information about the subsurface conductivity structure at a large variety of depths. Generally, inductive methods such as TDEM also have the advantage that they produce viable data when instruments are mounted on a moving platform, which may either be towed on-ground (Auken et al., 2019a,b), floating on a body of water (Auken et al., 2019b) or mounted on an air-borne frame (Witherly et al., 2004; Sørensen and Auken, 2004; Lane et al., 2000). This makes the method very versatile and useful for a large variety of applications, such as in environmental studies (Christensen and Halkjær, 2014), mapping of aggregate construction materials (Ellefsen et al., 1998), exploration for groundwater resources (Siemon et al., 2009; Minsley et al., 2021), and even for general geological mapping (Høyer et al., 2015).

Being able to properly model and calculate the physics of a TDEM sounding, the forward calculation, is crucial for the extraction of information from data through geophysical inversion. The TDEM method is based on Faraday's law of induction, which states that any magnetic field that varies in time is always associated with an electric field which also varies in both time and space. By passing a constant current through a conducting loop, a static magnetic field is induced. If the current is abruptly switched off, causing the magnetic field to quickly disappear, eddy-currents are induced in the subsurface which diffuse outwards and away from the loop source. Since these eddy currents produce their own time-varying magnetic field, usually referred to as the secondary field, an electromotive force will be exerted in the loop receiver. Data is obtained by measuring the value of this secondary electromotive force in a receiver loop as it varies in time, with early values predominantly associated with shallower eddy currents and later values associated with predominantly deeper eddy currents. Given some discretization of the subsurface, divided into a set of volumes with a constant conductivity value within each volume and sufficient computational resources, it is possible to calculate an approximation to this forward response under certain assumptions, usually by solving Maxwell's equations in the quasi-static approximation (Ward and Hohmann, 1987). However, this is often not feasible in practice, especially for large scale surveys, due to the high computational cost of the calculation (Bai et al., 2021; Deleersnyder et al., 2024). In practice many approaches instead rely on a forward calculation that assumes a laterally homogeneous 1D layered earth, greatly reducing the complexity of the calculation (Auken et al., 2015; Brodie, 2016; Heagy et al., 2017; Falk et al., 2025).

Given the widespread use of the 1D assumption it is important to keep in mind that it is never fulfilled. In situations where the subsurface structure cannot be approximated by a 1D model this assumption will introduce a 3D modeling error in the forward model, sometimes referred to as "geological noise" (Everett and Weiss, 2002). Often the presence of such 3D modeling errors may be identified by characteristic 3D artifacts in the inversion results, such as sharply dipping layer boundaries at the edges of lateral structure discontinuities, referred to as "pant-legs" (Goldman

et al., 1994). Other well documented 3D artifacts include the underestimation of layer boundary slopes (Danielsen et al., 2003), distortions of conductivity contrasts (Goldman et al., 1994) and the underestimation of the depth to the base of a buried valley structure (Bai et al., 2021). If not handled meticulously, these 3D modeling errors may produce geologically unrealistic models - or worse, geologically realistic models that are erroneous.

To the best of our knowledge, no studies comprehensively document the effects of 3D modeling errors on inversion results for models with more than 2 layers. Furthermore, while we know of no studies analyzing in detail the tempo-spatial structures of 3D modeling errors in TDEM or their impact on fit metrics such as the normalized data residual in least-squares inversion or the average likelihood of prior models, known as the evidence in probabilistic inversion, Xiao et al. (2023) does show how 3D modeling errors near a conductive saltwater shoreline affect the normalized data residual.

We document 3D modeling errors across both temporal and spatial domains, based on synthetic TDEM survey datasets across three different geological settings - a non-flat topography, a buried valley structure and a lens structure which is exposed at the surface. All three models have three layers with resistivities $20\Omega m$, $70\Omega m$, and $200\Omega m$. The analysis will cover all six possible permutations of the combination of these resistivities and the three layers for each geological type, so that there is a total of 18 different three-layer models. The aim of this study is to answer the following questions: how do 3D modeling errors, leading to 3D modeling errors, manifest for different resistivity structures in data and in inversion models, what role does variation in resistivity contrasts have in defining the answer to that question, and how are the goodness-of-fit measures influenced by the presence of 3D modeling errors?

THEORY

The Forward Problem

The forward problem in geophysics describes the relationship between model parameters and the theoretically predicted data. For a given set of model parameters $\mathbf{m}$, the forward operator F refer to the forward mapping from $\mathbf{m}$ to predicted data $\mathbf{d}$:

$$\mathbf{d} = F(\mathbf{m}) \tag{1}$$

In time-domain electromagnetics (TDEM), the forward operator solves Maxwell's equations in the quasi-static approximation to predict the transient electromagnetic response for a given subsurface resistivity distribution. This theoretical relationship is exact in the sense that it does not account for any errors or uncertainties.

Observed Data and Errors

In practice, observed data $\mathbf{d}_{obs}$ differ from theoretical predictions due to various sources of error:

$$\mathbf{d}_{obs} = F(\mathbf{m}_{true}) + \mathbf{n}(\mathbf{m}) \tag{2}$$

Here, $\mathbf{n}(\mathbf{m})$ represents the combined effect of all errors affecting the observed data. These errors can be broadly categorized into:

1. **Measurement noise**: Random fluctuations and systematic errors in the recording instruments
2. **Modeling errors**: Discrepancies between the theoretical model, F, and reality

In TDEM surveys, modeling errors are particularly significant when using simplified theoretical approximations, such as using a 1D forward model to approximate real-world 3D structures:

$$\mathbf{n}_{modeling} = F_{3D}(\mathbf{m}_{true}) - F_{1D}(\mathbf{m}_{true}) \tag{3}$$

Such 3D modeling errors may, if its amplitude is significantly high as compared to measurement noise, introduce systematic biases in the inversion results that appear as artifacts in the recovered resistivity models.

We consider two different approaches to inversion: deterministic and probabilistic methods.

Deterministic Inversion

The deterministic approach to solving the inverse problem typically involves minimizing an objective function consisting of data misfit and model regularization terms (Menke, 1989):

$$\Phi(\mathbf{m}) = \Phi_d(\mathbf{m}) + \lambda\Phi_m(\mathbf{m}) \tag{4}$$

Where:

- $\Phi_d(\mathbf{m}) = \|\mathbf{W}_d(\mathbf{d}_{obs} - F(\mathbf{m}))\|^2$ is the weighted data misfit
- $\Phi_m(\mathbf{m}) = \|\mathbf{W}_m(\mathbf{m} - \mathbf{m}_{prior})\|^2$ is the model regularization term
- λ is the regularization parameter balancing data fit and model constraints

- $\mathbf{W}_d$ and $\mathbf{W}_m$ are weighting matrices related to data and model covariances

The goal is to find a model $\mathbf{m}$ that minimizes $\Phi(\mathbf{m})$, typically through iterative optimization techniques. The solution depends critically on the chosen regularization and may be influenced by the starting model and inversion parameters.

Probabilistic Inversion

The probabilistic approach frames the inverse problem in terms of probability density functions. Following Tarantola's formulation (Tarantola and Valette, 1982; Tarantola, 2005), all information is expressed through probability densities:

1. Prior model information is represented by $\rho_m(\mathbf{m})$, incorporating any available constraints on model parameters.
2. Data information is represented through the likelihood function $L(\mathbf{m})$ the represent both measurement noise, $\rho_d(\mathbf{d})$, typically a Gaussian distribution centered on the measured values, $\mathbf{d}_{obs}$, with covariance reflecting measurement uncertainties, and modeling errors, represented by $\theta(\mathbf{d}|\mathbf{m})$.

The solution to the inverse problem is the posterior probability density function, that represents the combined state of information, which is given by combining the prior and data information as (Tarantola and Valette, 1982):

$$\sigma(\mathbf{m}) \propto \rho_m(\mathbf{m})\ L(\mathbf{m}) = \rho_m(\mathbf{m}) \int \theta(\mathbf{d}|\mathbf{m})\ \rho_d(\mathbf{d})\ \ d\mathbf{d} \tag{5}$$

Unlike deterministic inversion that yields a single "optimal" model, the probabilistic solution provides a distribution of models that reflects the combined state of information and associated uncertainties. In this framework, modeling errors can be explicitly incorporated in the likelihood function $\theta(\mathbf{d}|\mathbf{m})$, allowing for more robust interpretations that account for the limitations of the theoretical approximations.

In practice, however, modeling errors are often ignored or inadequately accounted for in the likelihood function. The typical assumption is that the theoretical relationship is exact, in which case $\theta(\mathbf{d}|\mathbf{m}) = \delta(\mathbf{d} - F(\mathbf{m}))$, where δ is the Dirac delta function. Then the posterior distribution becomes:

$$\sigma(\mathbf{m}) \propto \rho_m(\mathbf{m})\ \rho_d(F(\mathbf{m})).wa \tag{6}$$

This simplification, while computationally convenient, potentially leads to biased inversion results when significant modeling errors are present (Hansen et al., 2014).

The central aim of this paper is to investigate the consequences of ignoring modeling errors that arise from using 1D forward models to approximate 3D structures in TDEM. We systematically examine how these modeling errors manifest in inversion results using both deterministic and probabilistic approaches.

Goodness-of-Fit Measures

For both deterministic and probabilistic inversion approaches, we employ specific goodness-of-fit (GOF) metrics to evaluate how well models explain observed data in the presence of 3D modeling errors.

For the deterministic least-squares inversion, we use the normalized data residual (R_{norm}):

$$R_{norm} = \sqrt{\frac{1}{N}\sum_{i=1}^{N}\left(\frac{d_i^{obs} - F_i(\mathbf{m})}{\sigma_i}\right)^2} \tag{7}$$

where N is the number of data points, d_i^{obs} is the i-th observed data point, $F_i(\mathbf{m})$ is the corresponding forward response, and σ_i is the standard deviation of the assumed noise on the i-th data point. Values of $R_{norm} \approx 1$ indicate that data fit within the assumed noise level, while values significantly greater than 1 suggest systematic misfit potentially caused by modeling errors.

For the probabilistic inversion, we use the evidence ratio (E_{ratio}):

$$E_{ratio} = \frac{E(\mathbf{d}_{1D})}{E(\mathbf{d}_{3D})} \tag{8}$$

where $E(\mathbf{d})$ is the evidence (marginal likelihood) for dataset $\mathbf{d}$, representing the average likelihood of prior models, which can be estimated directly from likelihoods computed for all the prior model realizations in the lookup table. This ratio quantifies how much more difficult it is to fit $\mathbf{d}_{3D}$ compared to $\mathbf{d}_{1D}$ within the probabilistic framework. Values significantly more than 1 indicate that the 3D data are systematically harder to explain with the 1D forward model.

METHODS

Geological Models

We analyze 3D modeling errors for three specific three-layer models with combinations of resistivities of $20\Omega m$, $70\Omega m$ and $200\Omega m$. The three model types imitate geological structures: a buried valley, a surface lens, and varied topography. For each geological type, we examine all six possible permutations of the three resistivity values across the layers, resulting in a total of 18 different models for analysis. Across these models, we simulate TDEM measurements along profiles consisting of 51 soundings. The profiles span 1000m for the lens and topography models, while the buried valley model utilizes a 1500m profile. Each model is parameterized using continuous functions that define the depths of layer boundaries, creating the desired geological layer structures. For numerical simulation, we map these continuous models onto discrete mesh-grids, assigning appropriate resistivity values to cells between layer boundaries. If a layer boundary passes through a cell we take the volume weighted mean conductivity of

the layers present within the cell. The layer boundary modeled for each geologic type are illustrated in Figure 1.

Buried Valley

The buried valley model is, contrary to the other models, a 2D symmetric model. The function describing the depth to the valley boundary is given below:

$$d_{valley}(x) = \begin{cases} \left(\left(\frac{2x}{W} \right)^2 - 1 \right) \cdot D - D_0 & \text{for } |x| \leq W/2 \\ -D_0 & \text{for } |x| > W/2 \end{cases} \tag{9}$$

The valley is defined by a width, W, a depth to the valley top, D_0, and a depth from the top to the bottom of the valley, D. We use $W_{valley} = 500m$, $D_0 = 24m$, and $D = 48m$. These buried valley parameters are highlighted in the conceptual drawings in Figures 1a and 1d.

Surface Lens

The surface lens model is parameterized using a hyperbolic tangent function in the x and y dimensions, that determines its thickness, T_{lens}:

$$T_{lens}(x, y) = T_{max} \cdot \frac{1}{2} \left(tanh\left(\frac{\sqrt{x^2 + y^2} - d}{w} \right) - 1 \right) \tag{10}$$

Where d is the radial distance from the origin to the middle-point of where the lens thickness changes from T_{max} to 0. This change in thickness primarily occurs in the distance interval from $d - w$ to $d + w$, measured from the origin, so w is the half-width of this interval. We use $w = 20m$, $d = 200m$ and $T_{max} = 9m$. These surface lens parameters are highlighted in the conceptual drawings in Figures 1b and 1e.

Topography

We parameterize the the z coordinate at the height of our topographic model in the form of a simple Gaussian function in the x and y dimensions, with an isotropy parameter, a, which determines the lateral shape of the topographic structure:

$$H_{topography}(x, y) = H_{max} \cdot exp\left(-8 \frac{x^2 + a \cdot y^2}{(W_{topography})^2} \right) \tag{11}$$

Here, $x = 0$ and $y = 0$ are the x- and y-coordinates of the center point around which the structure is symmetrical in the x and y directions, and is simultaneously where the topography is at its heighest elevation, given by H_{max}. The approximate width of the structure in the x-direction is W and $\frac{W}{\sqrt{a}}$ in the y-direction. We use $W_{topography} = 300m$, $H_{max} = 15m$, and $a = 0.25$. These topography parameters are highlighted in the conceptual drawings in Figures 1c and 1f.

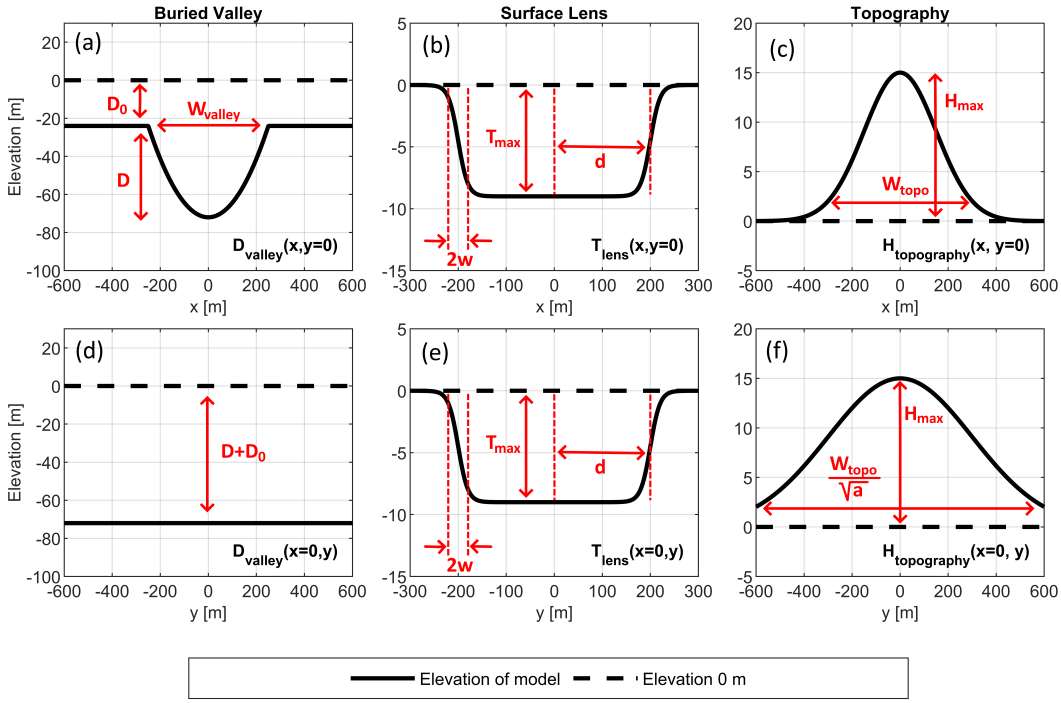

Figure 1: The geological models are defined by the functions $D_{valley}(x, y)$, $T_{lens}(x, y)$, and $H_{topography}(x, y)$. Relevant parameters for each model type are indicated on the panels. Panels (a) to (c) show the three models along the x-direction, keeping y = 0 fixed. Panels (d) to (f) show the three models along the y-direction, keeping instead x = 0 fixed.

Forward Modeling

All 3D TDEM forward modeling is done with SimPEG, which is a python-based open-source library for simulation and parameter estimation in geophysics (Cockett et al., 2015). SimPEG is particularly useful for the simulation of electromagnetic geophysics (Heagy et al., 2017). When quantifying the 3D modeling error, we use the 3D TDEM forward algorithm to predict both data from a 3D geological model and the 1D equivalent horizontally homogeneous model. We use 1D forward modeling only for the 1D inversion algorithms and to benchmark the 3D forward algorithm. Both the deterministic least-squares inversion and the probabilistic inversion algorithms use

AarhusInv for 1D forward modeling (Auken et al., 2015; HGG, 2017). This choice of forward algorithm was made because it is already implemented in the AarhusInv least-squares inversion algorithm, and choosing the same forward algorithm for the probabilistic inversion was convenient and practical, ensuring that differences between the two are minimized.

The TDEM system

We model a simple TDEM system consisting of a circular transmitter of area $1m^2$ with a central-loop vertical dipole receiver. The waveform is a trapezoid with ramp-on from -1.9×10^{-3}s to -1.8×10^{-3}s and ramp-off from -1 $\times 10^{-5}$s to 0s. We model 30 logarithmically spaced dB_z/dt values at points in time ranging from 1.0×10^{-5}s to 1.0×10^{-2}s.

Discretizing the mesh and time steps

We utilize SimPEGs OcTree meshing capability for the model grid used in the 3D TDEM forward calculations, which is an adaptive meshing method where the modeling domain can be discretized by cubic cells (Cockett et al., 2015). In regions where mesh refinement is required, individual cells may be split into 8 cubic cells of equal size, where the original cell is considered the parent cell, hence the tree structure. Typically, one should refine the mesh in areas where high accuracy is needed and/or the electromagnetic fields are rapidly changing in time or in space, such as near the TEM source or receiver. Refinement may also be required to accurately capture the geometries of the geological model itself. Because the optimal mesh refinement depends on the application we have designed three different OcTree meshes which are illustrated in Figure 2, one for each geological model. Our base cell-size is $3m$, which is used near the source-receiver pair, and as the distance to the instrument gets larger, so does the mesh-grid cell size, reflecting the dissipating sensitivity of the TDEM method with depth. The mesh refinement designed to capture the model geometry is the primary difference between the grids, which all have a total domain width and height of 12,288m. The mesh-grids for a buried valley, a surface lens and topography contain 34980, 37108 and 77540 cells, respectively. The number of time steps is 1623, of which half, 818, are during the waveform, primarily close to the current ramp-off. The smallest time step is $8 \times 10^{-8}s$, for the last 10 microseconds of the waveform, covering the ramp-off, and for the first 10 microseconds, until the first measurement at $1 \times 10^{-5}s$, The size of time steps then gradually increase, reaching a maximum of $4.3 \times 10^{-5}s$.

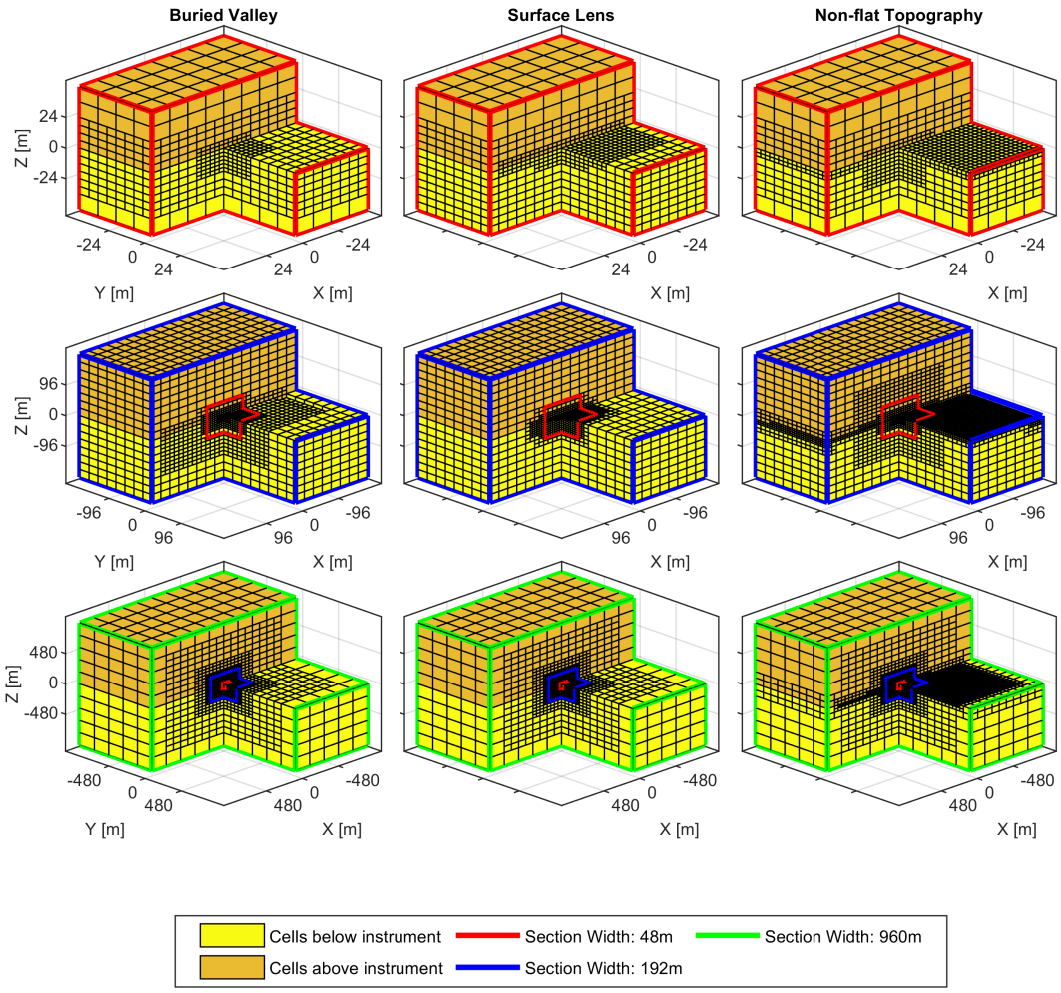

Figure 2: Sections of the octree mesh-grids used for each of the three geologic models. Yellow cells indicate cells below the instrument, $z_{cellcenter} < 0$, while the orange cells are above the instrument, $z_{cellcenter} > 0$. Outlines indicate the shown sections, where red is $48m$ wide, blue is $192m$ wide, and green is $960m$ wide. The black appearance at some parts of each mesh-grid is due to a high density of cell edges.

The challenge of modeling topography

The topography mesh requires significantly more cells than other model types due to inherent limitations of the OcTree mesh structure when representing smooth, curved surfaces. OcTree meshes, while computationally efficient, use cubic cells that create a 'stair-step' approximation of curved boundaries. This becomes particularly problematic when modeling electromagnetic responses over gradually sloping terrain. Using the standard approach of mapping a geological model with smooth topography onto an OcTree mesh with a fixed Cartesian coordinate system would result in artificial discontinuities as the modeled instrument moves across cell boundaries, creating abrupt elevation changes rather than smooth transitions along the surface. To handle this issue, we map the geological model onto a mesh where the coordinate system has been transformed by translation along x and z, so that the instrument is always located in $(x_{mesh}, z_{mesh}) = (0, 0)$ and then by a rotation, equal to the topographic slope at the instrument, getting the topography to be horizontal in the vicinity of the instrument. For the case of our topographic model and choice of mesh, the vicinity in which the horizontal within the mesh would approximately follow the slope was about 25 meters in each direction. We expect that this approach would not work as well for models with larger gradients, since that would reduce this distance. There is one major downside to this solution, which is that we must now design the mesh to capture the fact that the surface is sloping in the entire modeling domain, introducing a need for larger mesh refinement at large distances compared to solution 1. We chose solution 2 and found that the surface of the model could be adequately refined with cell sizes of 3m, 6m, 12m, and 24m to distances in both the x and y directions of 100m, 250m, 500m, and 1000m, respectively. The cost of this is an approximate doubling in the number of cells for the topographic mesh compared to the other two mesh-grids where this extra refinement is not used.

Validating the 3D Forward

To validate the accuracy of the 3D forward, we have bench-marked it against the semi-analytical solutions for laterally homogeneous models provided by the AarhusInv 1D forward algorithm. The geological models used in the analysis have layer boundaries at various depths, ranging from 3 m to 144 m, and we decided to test the 3D forward algorithm on two-layer models with boundary depths at 3m, 12m, 24m, 48m, 96m, and 144m. Furthermore, given the three possible layer resistivities, $20\Omega m$, $70\Omega m$ and $200\Omega m$, there is a total of 6 unique resistivity combinations for each of the 6 depths, corresponding to 6 unique resistivity contrasts. Hence, we bench-mark the algorithm against a total of 36 different two-layer models. The 3D forward as set up here generally produces relative differences lower than 3%, as shown in Figure 3, which is the level of accuracy that we aimed for during development of the individual mesh-grids. For depths 3m and 12m we test the lens mesh, for depths 24m and 48m we test the topography mesh, and for depths 96m and 144m we test the buried valley mesh. A few models produced relative deviations above the target, where the

models with high deviations in the early times all had the boundary depth at $3m$, with the largest error associated with a conductive upper layer and resistive lower layer. Meanwhile, the models with high deviations at late times were associated with a resistive lower layer and a shallow layer boundary.

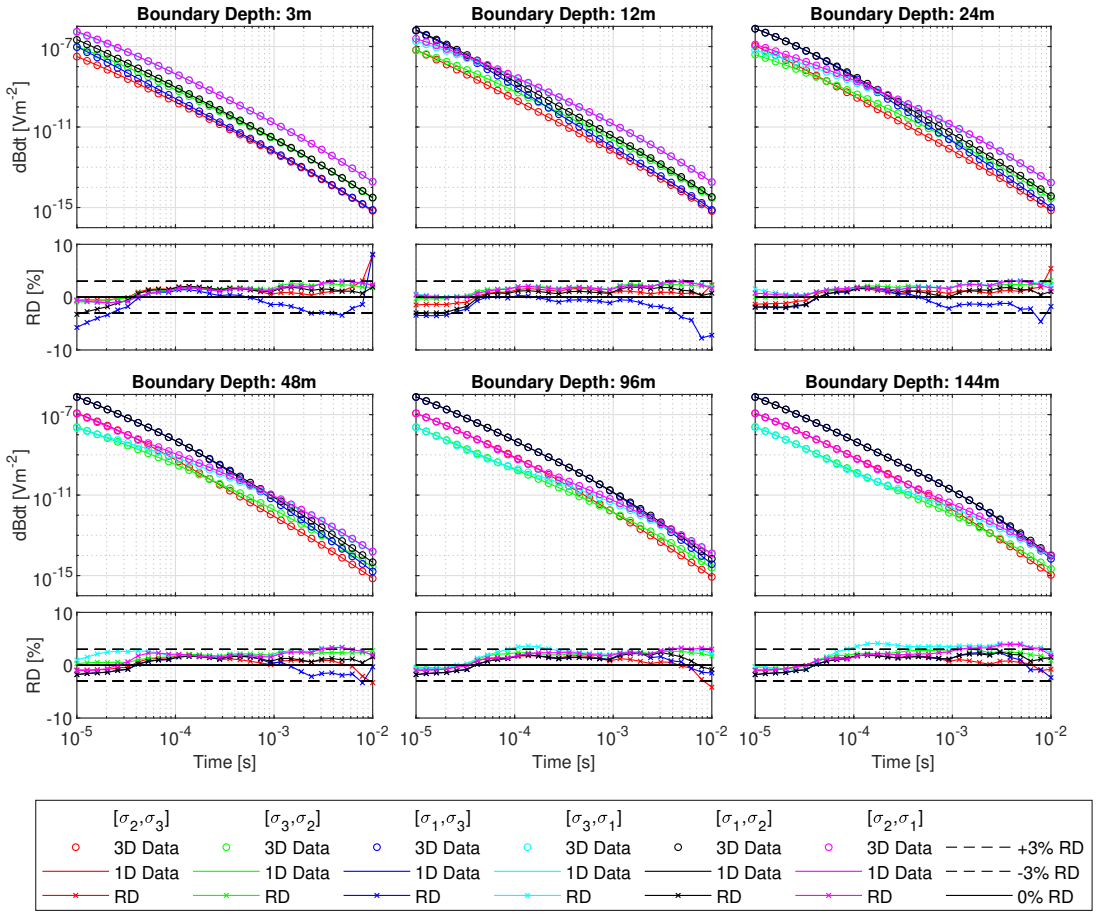

Figure 3: Results for bench-marking the 3D forward against the semi-analytical 1D forward from AarhusInv on two-layer models with the boundary at different depths and for various resistivity contrasts. Generally, the relative deviation is below 3%. The circles show the predicted data from the 3D forward while the solid lines show the corresponding result using AarhusInv. The lines with cross-markers show the relative deviation between the two forward algorithms while the black dashed lines show a relative absolute deviation of 3% for reference.

The 3D modeling error

The 3D modeling error for one single sounding is quantified by the relative deviation (RD), measured in percent, between the 3D forward response and the 1D forward response.

$$RD_{1D/3D} = 100 \cdot \frac{d_{1D} - d_{3D}}{d_{3D}} \tag{12}$$

This may be calculated using d_{3D} from the 3D response obtained with SimPEG and d_{1D} as produced by AarhusInv for example. However, when quantifying this relative absolute deviation, the result is not purely the 3D modeling error, but instead a combination of any modeling errors that are not the same between the two responses, for example errors that relate to the mesh in the 3D forward algorithm. As seen in Figure 3, these differences can be assumed to be at least a few percent. We have therefore also chosen to calculate the 1D forward response using the SimPEG 3D forward at the cost of extra computation time, taking the 1D model at the sounding location and propagating it onto the entire grid. With this setup the modeling errors are expected to be the same for both d_{1D} and d_{3D}, canceling in the RD calculation. The remaining difference is assumed to be the 3D modeling error only.

Inversion Algorithms

We invert both the data with and without 3D modeling errors, d_{3D} and d_{1D}, respectively, using probabilistic and deterministic inversion algorithms. The goal is to show how the choice of inversion framework influences the resulting 3D artifacts, and it is not the goal to directly compare the algorithms. This approach highlights the general manifestation of 3D modeling errors through artifacts shared by inversion models obtained with different frameworks. Caution is advised when comparing deterministic and probabilistic methods, as their solutions represent fundamentally different concepts. Both inversion algorithms assume 3% uncorrelated Gaussian noise, though no noise is added, to isolate the impact of 3D modeling errors under ideal conditions.

Deterministic Least Squares Inversion

For the deterministic inversion we use the a linearized least-squares inversion algorithm as implemented in AarhusInv (Auken et al., 2015), which follows the formalism of Menke (Menke, 1989). AarhusInv minimizes the L_2 data and regularization misfit with Marquardt damping. We use only vertical constraints, such that individual soundings are inverted independently of each other, with an assigned variance of 1 for the difference in resistivity between adjacent layers in the 1D inversion model. We use a 30-layer model with fixed layer boundaries extending to $300m$ depth, and layer

thicknesses that gradually increase, starting at $3m$ for layer 1 and ending at about $20m$ for layer 29. The inversion starting model is $30\Omega m$ for all layers.

Probabilistic Inversion

For the probabilistic inversion, we use the extended rejection sampler Hansen (2020) to sample the posterior distribution. It makes use of lookup-table containing a finite sample from the prior distribution of 1D resistivity models as well as the corresponding 1D TDEM forward responses (prior data). Each prior model is accepted as a realization of the posterior distribution proportional to the likelihood of each corresponding prior data. This method can be efficient because we solve the inverse problem repeatedly using the same prior distribution, hence the look-up table neeeds to be computed only once. This, in turn, allows for the usage of quite a large sample from the prior distribution. However, it is possible that in some cases it is hard to find a model that fits data, even for very large samples from the prior, so it is important to evaluate the posterior sample to ensure that it consists of a suitable minimum number of unique realizations from the prior, such that it adequately represents the posterior distribution shape.

The prior distribution used contains models that all have 4 layers, with boundaries following a log-normal distribution in the depth interval from $1m$ to $1000m$. Layer resistivities are similarly drawn from a log-normal distribution in the interval from $1\Omega m$ to $1000\Omega m$, independently from the depth of each layer boundary.

RESULTS

For each of the three geological models, and for each of the six different combinations of layer resistivities, making a total of 18 different reference models, we show the inversion models for d_{3D} given both the probabilistic and deterministic inversion algorithms. The results for the buried valley, surface lens and non-flat topography types are shown in Figures 4, 5, and 6, respectively. For each reference model we also show the relative deviation, RD, between d_{1D} and d_{3D} across all 50 sounding locations and for all 30 data points. Lastly, we show how the goodness-of-fit measure for each inversion algorithm changes along the simulated profile for each reference model.

Generally, it is worth noting that the magnitude of the 3D modeling error is greatest for models where the layer boundary causing the error is placed between layers with a large conductivity contrast, and the 3D inversion artifacts tend to be more pronounced when the most resistive layer is below the other two layers. Furthermore, it is also generally the case that positive 3D modeling errors cause artifacts that underestimate resistivity while negative 3D modeling errors cause artifacts that overestimate resistivity. For example, in the buried valley case, a large magnitude 3D modeling error and correspondingly well-defined artifacts are observed for model 3, which is the reference model in Figure 4a3, with the 3D modeling error having a

positive value right beneath the valley, where the artifact is underestimating resistivity in both the probabilistic and deterministic algorithms, and negative right next to the valley, where the artifact is instead overestimating resistivity, as shown in Figure 4b3 through 4d3. Models 4 and 6 consistently show no notable inversion artifacts for the three geological types, which is consistent with these models having the lowest 3D modeling errors as shown in Figures 4d,5d, and 6d.

There is a general tendency for the goodness-of-fit measures to be mostly affected by negative 3D modeling errors, as seen in Figure 4d1, 4d2, 4d3, and 4d5, but not in a consistent manner. For example, buried valley models 3 and 5 have similar negative 3D modeling errors outside of the buried valley extent, as seen in Figure 4d3 and 4d5, but the data residuals and evidence ratios in this region are hardly affected for model 5, despite its significant 3D inversion artifacts, while for model 3 the GOF measures are more affected. The increase in the GOF measures is generally also relatively small for all models, where 3D modeling errors seem to cause an increase in data residuals between only 0 and 1 for the deterministic inversion and changes in the evidence ratio of a few orders of magnitude for the probabilistic inversion.

Buried Valley Model

Notable 3D artifacts occur for reference models 1, 2, 3 and 5. Models 1 and 2 exhibit a vertical resistive structure below the buried valley with thinner and comparably more conductive structures below the valley flanks, as shown in Figures 4b1, 4c1, 4b2 and 4c2. For both the probabilistic and deterministic inversion algorithms, models 3 and 5 show a consistent overestimation of resistivity in the bottom layer in regions that appear near the valley flanks, as shown in Figures 4b3, 4c3, 4b5, and 4c5. However, they are more directly related to the region right outside of the valley, where they occur due to the discontinuity in the thickness of layer 2, caused by the buried valley. Furthermore, for these two models the resistivity is underestimated in a vertical region below the valley. This is consistent with the modeling error having a local amplitude maximum below the valley center (Figure 4d).

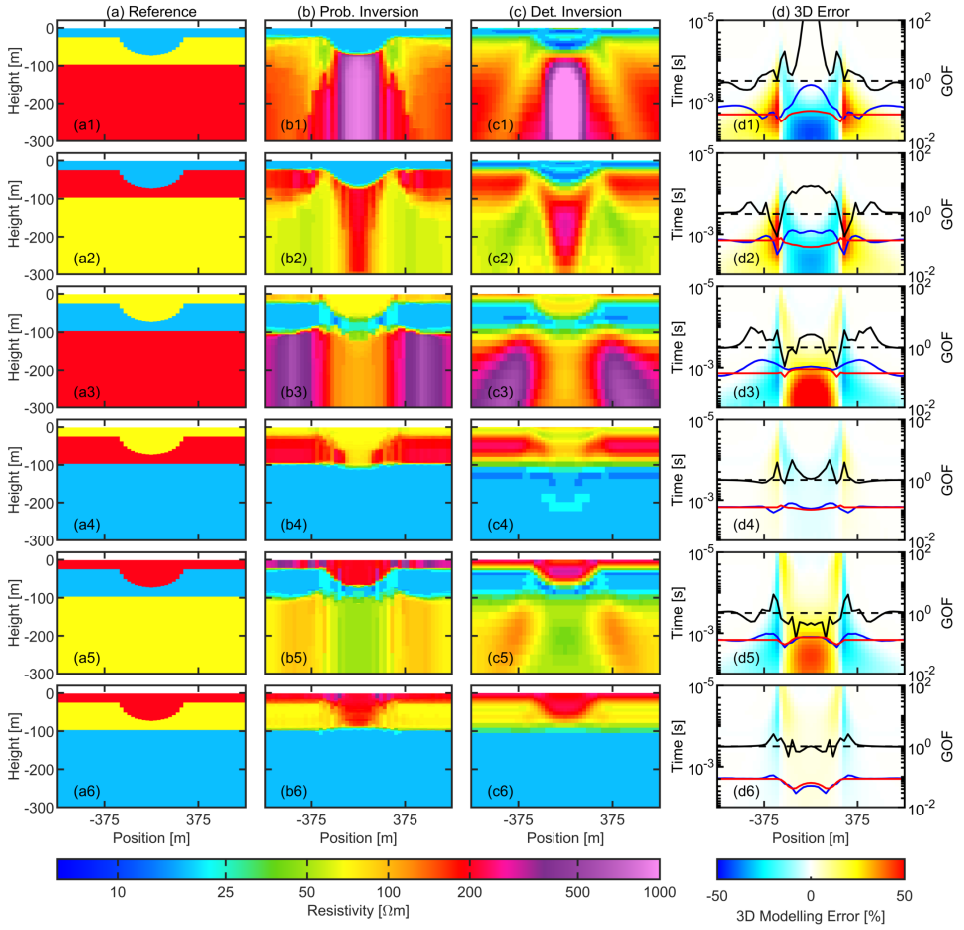

Figure 4: Models from inversion of the generated synthetic 3D TDEM data, d_{3D}, for the buried valley geological type along a 1 km profile. Column (a): reference models; (b): probabilistic inversion; (c): deterministic inversion; (d): 3D modeling error (RD) and GOF measures. The GOF measure for the probabilistic inversion, the ratio between the evidence metrics for d_{3D} and d_{1D} is shown with a black line while the GOF measure for the deterministic inversion, the normalized data residual, is shown in blue for d_{3D} and red for d_{1D}.

Surface Lens Model

The results for the surface lens geological structure are shown in Figure 5. Similarly to the buried valley models, notable 3D artifacts are seen for models 1, 2, 3 and 5. In model 1, Figures 5b1 and 5c1 show that the artifact manifests as a highly resistive region below the lens, alongside a distortion of the location of the boundary between layers 2 and 3. The geometries of the resistive region and the layer boundary distortion appear well-defined for the deterministic inversion (Figure 5c1) and less well-defined for the probabilistic inversion (Figure 5b1). Model 2 shows a different artifact geometry, where the dominant effect is the distortion of the boundary between

layers 2 and 3, which is clearest in the probabilistic inversion result (Figure 5b2). This is accompanied by a relatively small overestimation of the resistivity beneath the valley, which is mostly visible in the deterministic inversion result (Figure 5c2). The results for models 3 and 5 show regions with overestimated resistivity within the third layer directly outside of the lens structure, which are more visible in the deterministic inversion models, as shown in Figures 5c3 and Figure 5c5. Right beneath the lens structure the resistivity is first overestimated in a small region, and then instead it is underestimated in the deeper part. The initial overestimation of the resistivity is not a 3D artifact, we refer to Appendix A for details on why this is the case. The underestimation in the deeper part is, however, a 3D artifact.

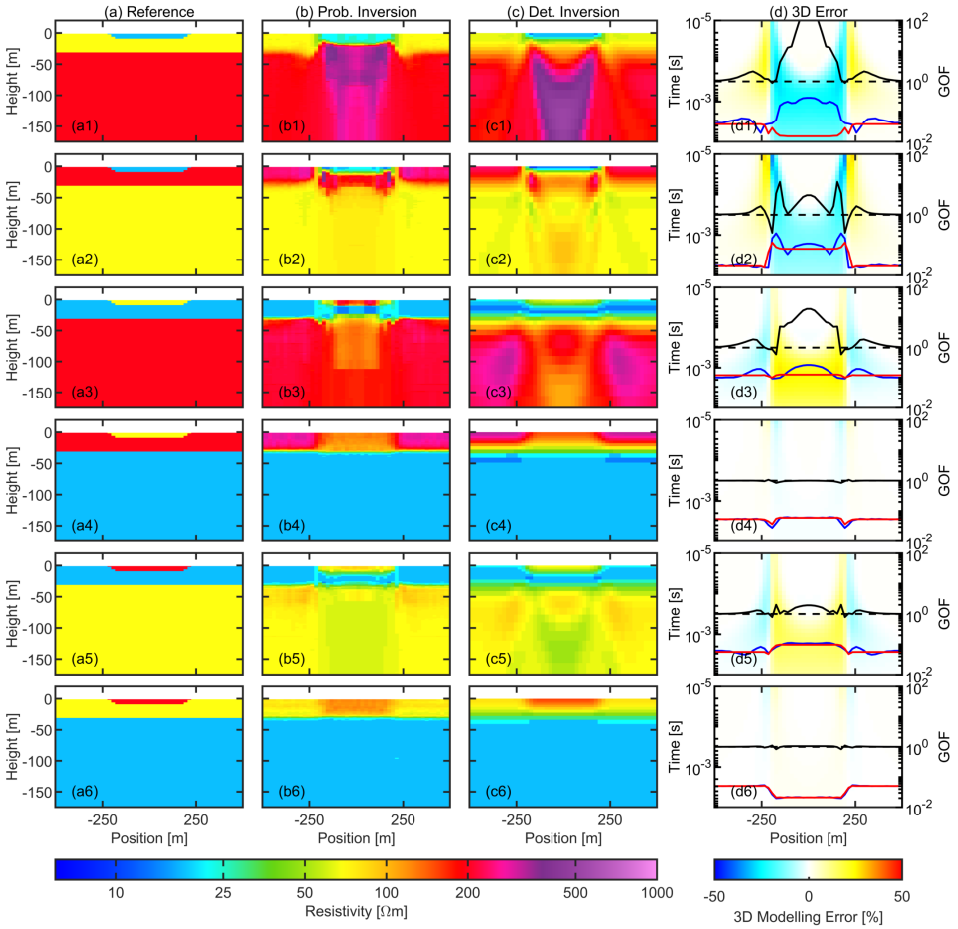

Figure 5: Models from inversion of the generated synthetic 3D TDEM data, d_{3D}, for the lens geological type along a 1 km profile. Column (a): reference models; (b): probabilistic inversion; (c): deterministic inversion; (d): 3D modeling error (RD) and GOF measures. The GOF measure for the probabilistic inversion, the ratio between the evidence metrics for d_{3D} and d_{1D} is shown with a black line while the GOF measure for the deterministic inversion, the normalized data residual, is shown in blue for d_{3D} and red for d_{1D}

Topography Model

The results for the six topography models are shown in Figure 6. Models 1,2,3 and 5 show notable 3D artifacts. In contrast to the results for buried valleys and the surface lens structure, all models for the topographic type is dominated by one central 3D artifact, while those on the flanks of the topographic structure are of comparably low amplitude, as shown in Figure 6d. It is also worth noting that this central modeling error is always negative because the surrounding material is air which has an extremely large resistivity. Figures 6b1 and 6c1 show that for model 1 the artifact is a highly resistive structure ($\rho > 1000\Omega m$) in the otherwise quite resistive ($\rho = 200\Omega m$) last layer. For model 2 the effect is a slight exaggeration in the thickness of layer 2, alongside a slightly more resistive region in the last layer, as can be seen in Figure 6b2 and 6c2. The less resistive region in the top of layer 3 on the flanks of the topographic structure is not a 3D artifact, but instead a characteristic of the deterministic inversion, we refer to Appendix A for documentation. Model 3 shows a resistive region below the structure (see Figure 6c3), similar to model 1, but the effect is reduced due to the higher resistivity ($\rho = 70\Omega m$) of the first layer compared to model 1, where it is $20\Omega m$. Interestingly, for model 3 the probabilistic inversion does not show the same artifact (see Figure 6b3). Models 4, 5 and 6 do not display any appreciable 3D modeling errors, and correspondingly no artifacts are presented (Figures 6d4, 6d5, and 6d6).

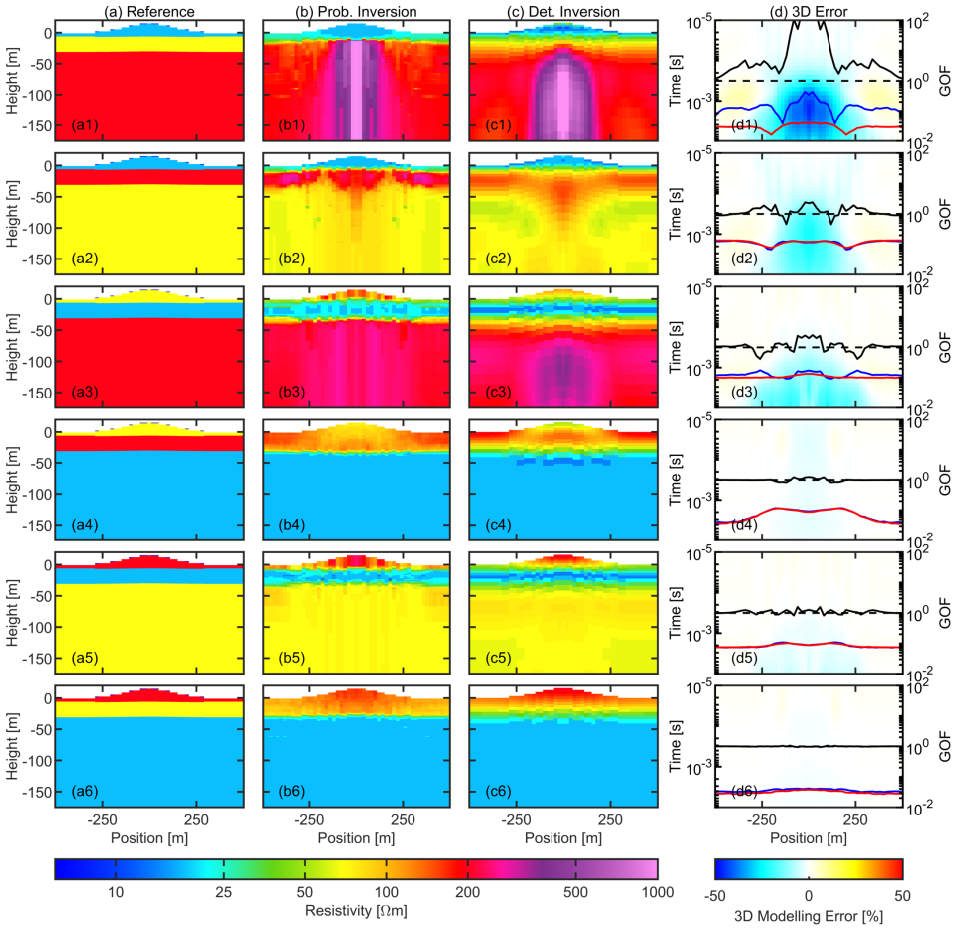

Figure 6: Models from inversion of the generated synthetic 3D TDEM data, d_{3D}, for the topography geological type along a 1 km profile. Column (a): reference models; (b): probabilistic inversion; (c): deterministic inversion; (d): 3D modeling error (RD) and GOF measures. The GOF measure for the probabilistic inversion, the ratio between the evidence metrics for d_{3D} and d_{1D} is shown with a black line while the GOF measure for the deterministic inversion, the normalized data residual, is shown in blue for d_{3D} and red for d_{1D}

CASE: POSSIBLE 3D ARTIFACTS IN A DANISH TDEM DATASET

To demonstrate the inherent value of understanding 3D modeling errors and their associated artifacts, as provided in this paper, we present a real case from Ribe in Southern Denmark, where inversion models from data acquired in a SkyTEM survey displayed unexpected resistive ellipsoidal features. The survey was commissioned by the local supplier of drinking water, DIN Forsyning, and was carried out for the purpose of mapping groundwater resources.

This airbone TDEM survey was done with typical flying altitudes of 30m to 60m, sounding spacings of 20m and line spacings of 200m, with the direction of flight lines striking north to south. The lines are shown in Figure 7a. The dual-moment SkyTEM306 system was used with a low moment of approximately $2700Am^2$ and a high moment of approximately $470000Am^2$. Measurements for the low and high moments were made in the interval $7.6\mu s - 474\mu s$ and $0.079ms - 10.6ms$, respectively (SkyTEM, 2025; Sørensen and Auken, 2004). After acquisition of the airborne TDEM data and subsequent processing, it was inverted with the deterministic linearized least-squares algorithm AarhusInv (Auken et al., 2015). The inversion was spatially constrained (Viezzoli et al., 2008) and parameterized with 30 layers, where the first has thickness 4m, increasing logarithmically with depth until the last layer boundary which is located at 500m. All layer boundaries are fixed. The inversion result revealed unusual ellipsoidal resistive features, embedded within a relatively less resistive unit of approximate thickness 150m, as shown in Figure 7b-d.

In Figure 7a we show three selected profiles from the inversion model, denoted Line 1, 2 and 3, and highlighted in red. The corresponding inversion model profiles are shown in Figure 7b, 7c, and 7d. We chose these three profiles because they illustrate both the variety and abundance of the unexpected structures. The unit in which the structures are visible is located directly below a highly conductive layer with a thickness up to $35m$. Similarly, below the unit we also observe a highly conductive layer. The conductive layers seem to have average resistivities well below $10\Omega m$ while the resistive unit in between seems to vary a lot with resistivities between $40\Omega m$ and $80\Omega m$.

We propose that many of the structures observed in this dataset are inversion artifacts, caused by 3D modeling errors introduced by lateral variations in the thickness of the upper conductive layer due to erosional features such as buried valleys. For example, looking at lines 1 and 2 in Figure 7b and 7c and around UTM Y coordinate $6.135 \cdot 10^6 m$, two ellipsoidal structures seem to be located on each side of a more than 100m deep buried valley structure. This resembles the 3D artifacts in Figure 4d3 and 4d5. Furthermore, in these regions the data residual is generally below 1, with a peak in the residual near the northern side of the valley where the ellipsoidal structure is more pronounced. This is consistent with expectations if we hypothesize that the structures are indeed 3D artifacts. We can justify this claim by reference to the blue curve in Figure 4d3 where only a slightly elevated residual occurs at the artifacts below the valley flanks. Interestingly, for comparison in Figure 4d5 there is no discernible increase in residual, although the only difference between the models is the magnitude of the resistivity contrast between layers 2 and 3. Though, due to the small change in the residual one should be careful to use it as any sort of indicator for 3D modeling errors. Another interesting section is seen in line 2, Figure 7c, around UTM Y coordinates $6.140 \cdot 10^6 m$, where some sort of erosional feature at the surface has been filled with a resistive material. It is unclear how much, if any, of the conductive layer below remains, and ellipsoidal structures beneath the sides of the feature can be observed with an apparently increased resistivity. This occurrence of an erosional feature in conductive host sediments and resistive infill is similar to the

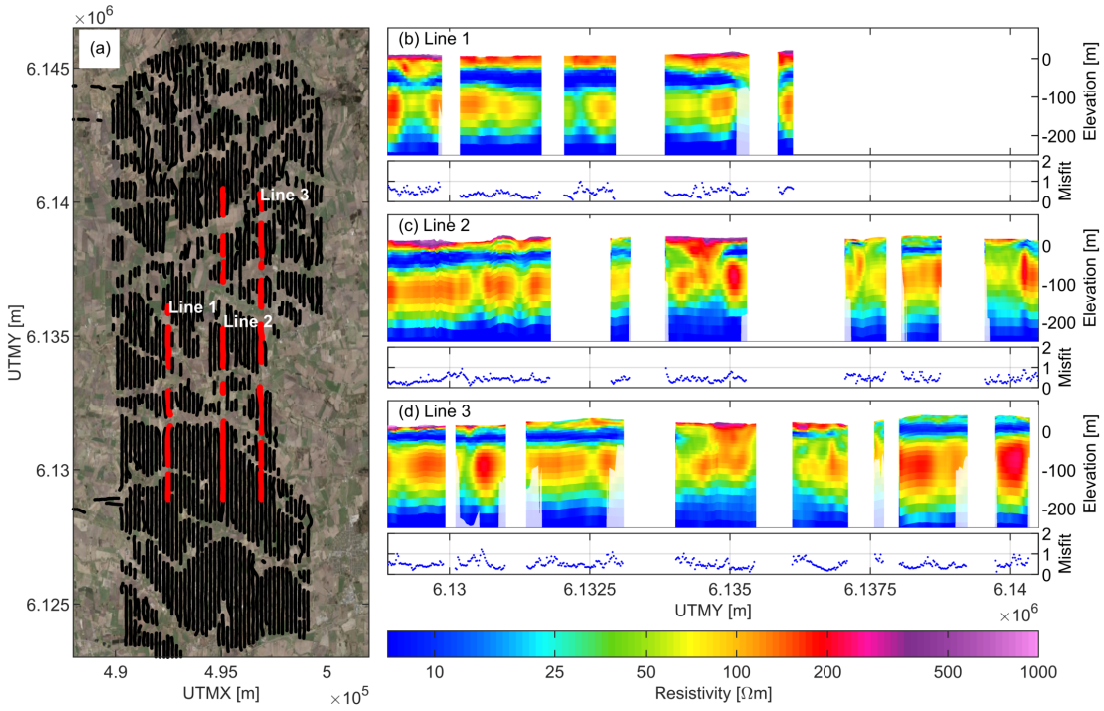

Figure 7: A SkyTEM Survey in Ribe, Southern Denmark, shows unexpected localized structures within a thick and relatively resistive Miocene unit. (a) shows the survey area with flight lines in black and three specific lines highlighted in red, denoted Line 1, 2 and 3. (b) shows the inversion model for line 1, (c) shows the inversion model for line 2 and (d) shows the inversion model for line 3. Models are blinded with a transparent white shading below the depth-of-investigation (DOI). The smaller axes below (a), (b) and (c) show the corresponding data misfit in the form of a data residual, normalized by the data uncertainty, for each sounding along the lines. White shading is used for blinding in areas below the depth-of-investigation (DOI).

model shown in Figure 5a5, and the observed structures in the layer below resemble the corresponding 3D artifacts in Figure 5d5. Again, the data residual is not elevated, which is consistent with the results in Figure 5d5. A similar example can be seen in Line 3, Figure 7c, near UTM Y= $6.130 \cdot 10^6 m$.

DISCUSSION

The inversion results show good agreement in the manifestation of the 3D artifacts between the deterministic and probabilistic inversion algorithms. However, a lot of the differences between the two are important to understand. For example, in the deterministic least-squares inversion the artifacts are easily visible, but layer boundaries manifest as smooth transitions. In contrast, the probabilistic inversion algorithm appears to recover sharp layer boundaries, which is possible because the prior models are 4-layer models with sharp layer boundaries.

Another difference between the two algorithms is that the deterministic inversion algorithm as applied here will readily fit data to an extent consistent with an assumption of a lower noise amplitude, if possible, causing the deterministic result to appear more well-defined than might be dictated by the noise model. This is also allowed in our analyses by the fact that we are overestimating the amount of uncorrelated noise during inversion by not adding any to data, but still assuming 3% is present. This means that we would expect the artifacts to be more well-defined in the deterministic inversion models, as seen in the results, for example as seen in Figure 5 column c compared to column b. Furthermore, we expect more well-defined 3D artifact geometries from the probabilistic inversion if a lower noise magnitude is assumed. On a related note, it is important to remember that not every deviation between the retrieved model and the reference model is a 3D artifact. Other discrepancies can be caused by a variety of factors, such as a lack of resolution, the choice of prior model in the probabilistic algorithm and the vertical constraints in the deterministic inversion, to name a few.
We note that, as shown in Figures 4d1, 4d2, 4d3 and 4d5, the buried valley models have significant maxima at late times compared to the maxima outside of the valley flanks. When the second layer is the more conductive of the three layers, as is the case in Figures 4a3 and 4a5, this causes the 3D inversion artifacts below the valley to be at a larger depth than those next to the valley, also due to the generally faster diffusion of the induced currents through resistive layers compared to conductive layers. This may have implications for models where below the valley, shallower layers are more affected by the artifacts near the flanks and deeper layers by the artifact below the valley center. A similar difference in the timing of 3D modeling error peaks besides and directly below the structure is seen for the topographic model, but here the magnitude of the central peak is significantly larger than the ones next to the topographic structure, causing the 3D artifacts to primarily manifest directly below it.

In the case from Ribe we see structures resembling the buried valley type of 3D

artifact, for example at UTM Y = $6.129 \cdot 10^6 m$ on line 1 in Figure 7b, similar to reference models 3 and 5 (Figure 4d3 and 4d5). Here, we see a distortion of the layer directly below valley, which is expected to be relatively flat, but shows a local structure of high elevation below the valley, which then steeply transitions into a local structure of low elevation outside of the valley, and directly below the resistive artifacts that we argue are 3D artifacts. As such, there is good reason to argue that the observed variation of elevation in the top of the underlying conductive layer may also be a 3D artifact, where the layer is in reality close to flat but gets distorted through a pull-up effect in the region with a positive 3D modeling error and a push-down effect in the regions with a negative 3D modeling error.

Unfortunately, the results show that the 3D modeling errors are not always identifiable by analysis of the normalized data residual in deterministic inversion or the evidence metric for probabilistic inversion. In fact, the relative change in the data residual is so small that for none of the 18 models tested it exceeds a value of 1, which is the threshold beyond which the data residual variance is larger than dictated by the noise model. The evidence metric seems to be more impacted by the presence of 3D modeling errors, but only for a few models, and this might also change when using different priors or noise assumptions. Whether or not the evidence can be used to infer the presence of this type of modeling error remains uncertain. It cannot be ruled out that other 3D modeling errors than those tested might still cause a significant worsening of the goodness-of-fit, for example errors that are more localized, greater in amplitude or with other geometries.

The case study presented from Ribe in southern Denmark illustrates the need to understand what 3D artifacts might look like in TDEM inversion models. In particular, it is interesting that the presence of layers below the structures that cause 3D modeling errors have an effect on how the corresponding artifacts manifest. It is likely for this reason that previously documented 3D artifacts do not offer a satisfying explanation for the structures seen in the Ribe dataset, since these analyses usually rely on a 2-layer model with focus on the immediate vicinity of the 3D geological structure. However, it appears to be the case that the 3D artifacts labeled by Danielsen et al. (2003) as I, II, and III are essentially caused by the same type of modeling errors as those seen in Ribe and in Figures 4 and 5. Furthermore, we note that a very similar type of resistive structure is observed by Kidmose et al. (2025) in inversion models from deterministic inversion of TEM data. Here, in contrast to the Ribe case, the upper conductive layer is composed of lake sediments with a relatively horizontal upper boundary, and the variations in thickness occur instead due to variations in the boundary with the layer below. As such this geological type is more in line with model 2 for the buried valley and surface lens, and similar artifacts to those shown in Figures 4c2 and 5c2 are observed in their inversion models. The authors of the paper recognize some of these models as unrealistic and hypothesize that they may either be due to 3D modeling errors or IP effects. Our analyses support the hypothesis that at least some of the structures may be 3D modeling errors. Ultimately, if an interpreter of TDEM inversion models are able to identify 3D artifacts, then subsequent interpretations can be made on a more informed basis. For example, distorted layer

boundaries may be interpreted with a bigger emphasis on the interpreters knowledge of the geology rather than on the geometries seen in the model.

CONCLUSION

This study demonstrates the impact of not accounting for 3D modeling errors in time-domain electromagnetic (TDEM) 1D inversion results. By analyzing synthetic 3D datasets, representing three different geological scenarios, we document how these 3D modeling errors manifest in both deterministic and probabilistic inversion models. These artifacts may mislead an interpretation, as they are not reliably indicated by standard goodness-of-fit measures such as the normalized data residual for deterministic inversion or the evidence ratio, which reflects changes in the likelihood distribution, for probabilistic inversion. Furthermore, we introduce a case study from Ribe in southern Denmark, which highlights the real-world relevance of these findings, as inversion models exhibit structures that closely resemble the synthetic 3D artifacts observed in our results. This demonstrates the need for the consideration of 3D modeling errors in geophysical inversion of TDEM data, particularly when interpreting subsurface structures in regions where lateral variations in geology are expected.

APPENDIX A

INVERSION RESULTS FOR 1D DATA

In the inversion results of the simulated 3D data it is not necessarily simple to distinguish between 3D artifacts, distortions due to limitations in resolution, and structures that occur due to factors isolated to the inversion algorithm. The appendix Figures A-1, A-2, and A-3 show the inversion results for the synthetic data generated with the 1D forward algorithm, d_{1D}, and as such discrepancies in the results shown between the reference models and inversion models are due to factors other than 3D modeling errors. The inversion models shown are inherently unrealistic due to the 1D assumption, but they are useful when attempting to distinguish between 3D artifacts and other effects.

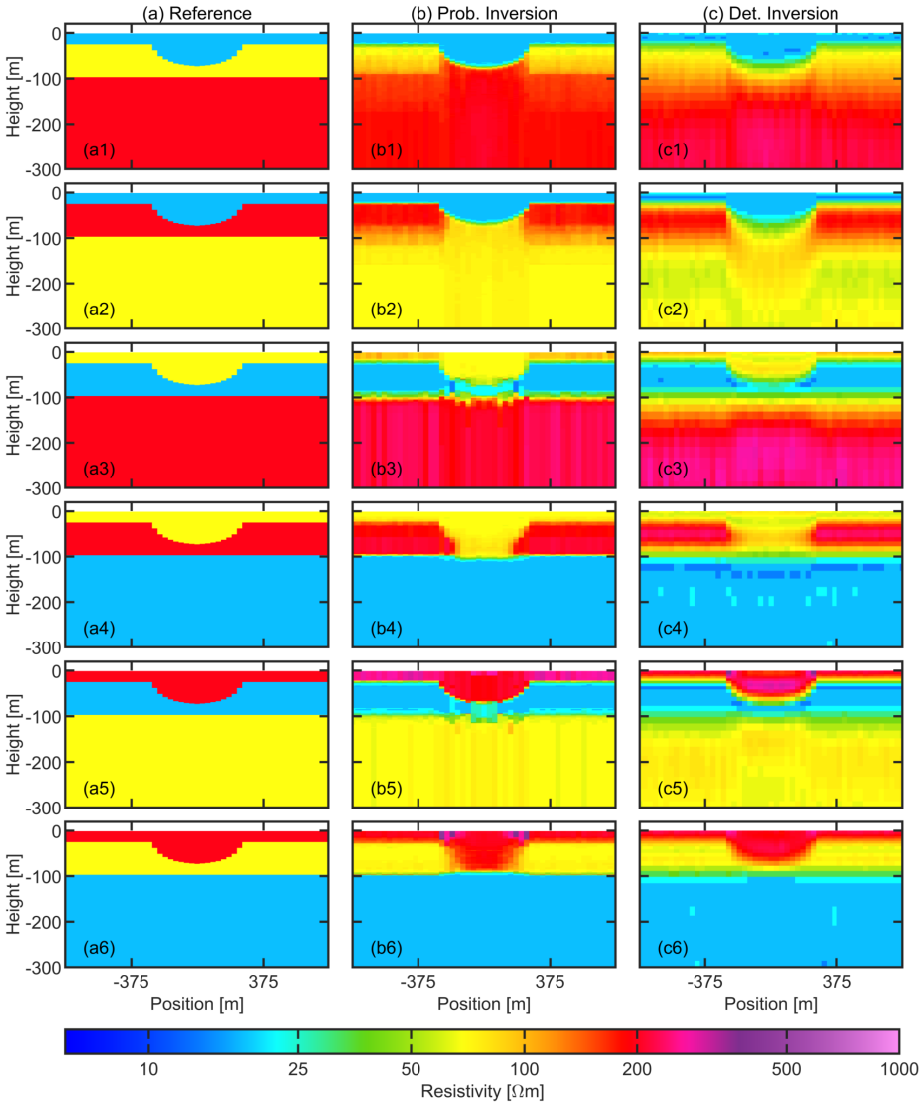

Figure A-1: Models from inversion of the generated synthetic 1D TDEM data, d_{1D}, for the buried valley geological type along a 1.5 km profile. Column (a): reference models; (b): probabilistic inversion results; (c): deterministic inversion results.

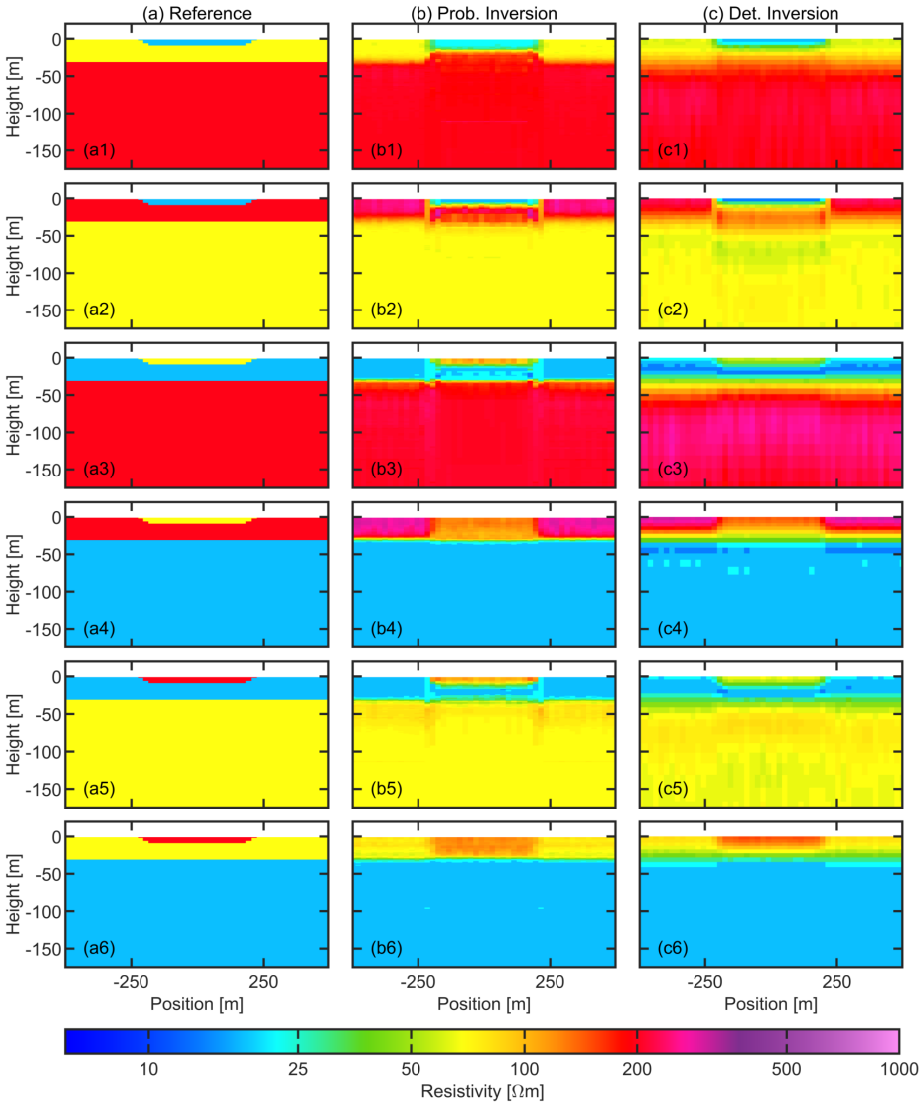

Figure A-2: Models from inversion of the generated synthetic 1D TDEM data, d_{1D}, for the lens geological type along a 1 km profile. Column (a): reference models; (b): probabilistic inversion results; (c): deterministic inversion results.

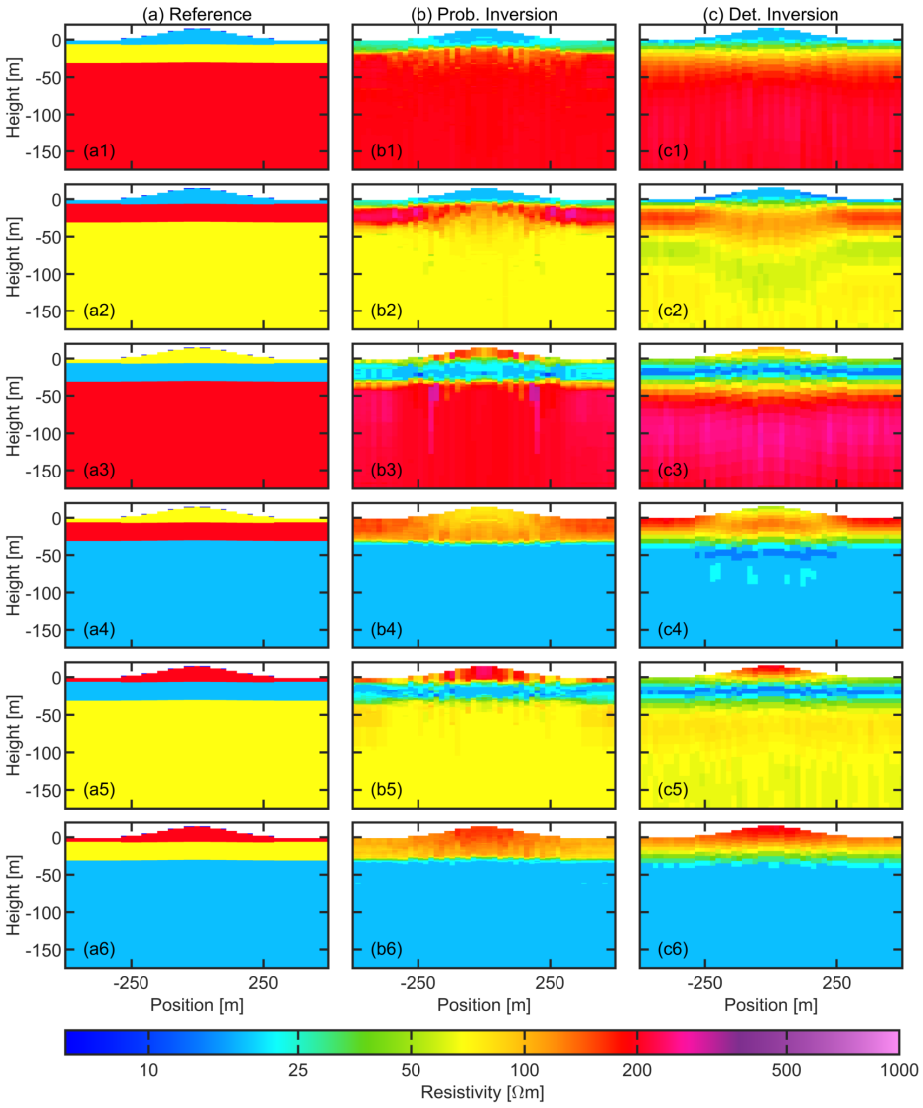

Figure A-3: Models from inversion of the generated synthetic 1D TDEM data, d_{1D}, for the topography geological type along a 1 km profile. Column (a): reference models; (b): probabilistic inversion results; (c): deterministic inversion results.

REFERENCES

Auken, E., A. V. Christiansen, C. Kirkegaard, G. Fiandaca, C. Schamper, A. A. Behroozmand, A. Binley, E. Nielsen, F. Effersø, N. B. Christensen, K. Sørensen, N. Foged, and G. Vignoli, 2015, An overview of a highly versatile forward and stable inverse algorithm for airborne, ground-based and borehole electromagnetic and electric data.

Auken, E., N. Foged, J. J. Larsen, K. V. T. Lassen, P. K. Maurya, S. M. Dath, and T. T. Eiskjær, 2019a, ttem - a towed transient electromagnetic system for detailed 3d imaging of the top 70 m of the subsurface: Geophysics, **84**, no. 1, E13–E22.

Auken, E., P. Maurya, A. Christiansen, J. Lane, E. White, and R. Adams, 2019b, A multipurpose platform towed tem-system imagining the top 100m of the subsurface; surface, water and snow: 25th European Meeting of Environmental and Engineering Geophysics, European Association of Geoscientists & Engineers, 1–5.

Bai, P., G. Vignoli, and T. M. Hansen, 2021, 1d stochastic inversion of airborne time-domain electromagnetic data with realistic prior and accounting for the forward modeling error: Remote Sensing, **13**, no. 19.

Brodie, R. C., 2016, User manual for geoscience australia's airborne electromagnetic inversion software.

Christensen, N. B., and M. Halkjær, 2014, Mapping pollution and coastal hydrogeology with helicopterborne transient electromagnetic measurements: Exploration Geophysics, **45**, no. 4, 243–254.

Cockett, R., S. Kang, L. J. Heagy, A. Pidlisecky, and D. W. Oldenburg, 2015, SimPEG: An open source framework for simulation and gradient based parameter estimation in geophysical applications: Computers and Geosciences, **85**, 142–154.

Danielsen, J. E., E. Auken, F. Jørgensen, V. Søndergaard, and K. I. Sørensen, 2003, The application of the transient electromagnetic method in hydrogeophysical surveys: Journal of Applied Geophysics, **53**, no. 4, 181–198.

Deleersnyder, W., D. Dudal, and T. Hermans, 2024, A multidimensional ai-trained correction to the 1d approximate model for airborne tdem sensing: Computers & Geosciences, **188**, 105602.

Ellefsen, K. J., J. E. Lucius1, and D. V. Fitterman, 1998, An evaluation of several geophysical methods for characterizing sand and gravel deposits.

Everett, M. E., and C. J. Weiss, 2002, Geological noise in near-surface electromagnetic induction data: Geophysical Research Letters, **29**, no. 1, 10–1–10–4. (Describes 3D errors as "Geological Noise" for Electromagnetic Induction Data).

Falk, F. A., A. V. Christiansen, and T. M. Hansen, 2025, Comparison of three one-dimensional time-domain electromagnetic forward algorithms: Applied Computing and Geosciences, **26**, 100243.

Goldman, M., L. Tabarovsky, and M. Rabinovich, 1994, On the influence of 3-d structures in the interpretation of transient electromagnetic sounding data: Geophysics, **59**, no. 6, 889–901.

Hansen, T. M., 2020, Efficient probabilistic inversion using the rejection sampler-exemplified on airborne em data: Geophysical Journal International, **224**, no. 1, 543–557.

Hansen, T. M., K. S. Cordua, B. H. Jacobsen, and K. Mosegaard, 2014, Accounting for imperfect forward modeling in geophysical inverse problems—exemplified for crosshole tomography: Geophysics, **79**, H1–H21.

Heagy, L. J., R. Cockett, S. Kang, G. K. Rosenkjaer, and D. W. Oldenburg, 2017, A framework for simulation and inversion in electromagnetics: Computers and Geosciences, **107**, 1–19.

HGG, 2017, Em1dinv manual. HydroGeophysics Group, Department of Geoscience, Aarhus University, Høegh-Guldbergs Gade 2, 8000 Aarhus C, Denmark.

Høyer, A.-S., F. Jørgensen, P. Sandersen, A. Viezzoli, and I. Møller, 2015, 3d geological modelling of a complex buried-valley network delineated from borehole and aem data: Journal of Applied Geophysics, **122**, 94–102.

Kidmose, J., S. Jessen, P. B. Sandersen, B. Nilsson, J. Koch, L. Thorling, J. B. Pedersen, A. V. Christiansen, and I. Møller, 2025, Remote sensing of preferential groundwater discharge with high-resolution geophysical measurements of floatem and ttem compared with lake surface temperature anomalies: Journal of Hydrology, **652**, 132523.

Lane, R., A. Green, C. Golding, M. Owers, P. Pik, C. Plunkett, D. Sattel, and B. Thorn, 2000, An example of 3d conductivity mapping using the tempest airborne electromagnetic system: Exploration Geophysics, **31**, 162–172.

Menke, W., 1989, Geophysical data analysis, discrete inverse theory: Academic Press.

Minsley, B. J., J. R. Rigby, S. R. James, B. L. Burton, K. J. Knierim, M. D. Pace, P. A. Bedrosian, and W. H. Kress, 2021, Airborne geophysical surveys of the lower mississippi valley demonstrate system-scale mapping of subsurface architecture: Communications Earth & Environment, **2**, 131.

Siemon, B., A. V. Christiansen, and E. Auken, 2009, A review of helicopter-borne electromagnetic methods for groundwater exploration: Near Surface Geophysics, **7**, no. 5-6, 629–646.

SkyTEM, Surveys, A., 2025, Transient electromagnetic (tem) systems, `https://skytem.com/transient-electromagnetic-tem-systems/`, accessed 2025-05-26.

Sørensen, K. I., and E. Auken, 2004, SkyTEM-A new high-resolution helicopter transient electromagnetic system: Exploration Geophysics, **35**, 191–199.

Tarantola, A., 2005, Inverse problem theory and methods for model parameter estimation: SIAM.

Tarantola, A., and B. Valette, 1982, Inverse problems= quest for information: Journal of Geophysics, **50**, 159–170.

Viezzoli, A., A. V. Christiansen, E. Auken, and K. Sørensen, 2008, Quasi-3d modeling of airborne tem data by spatially constrained inversion: Geophysics, **73**, no. 3.

Ward, S. H., and G. W. Hohmann, 1987, Electromagnetic methods in applied geophysics: Society of Exploration Geophysicists, volume **3** *of* Investigations in geophysics.

Witherly, K., R. Irvine, and E. B. Morrison, 2004, The geotech vtem time domain helicopter em system: 2004 SEG Annual Meeting, Society of Exploration Geophysicists, 1–4.

Xiao, L., G. Fiandaca, P. K. Maurya, and A. V. Christiansen, 2023, 3d inversion of

an integrated ground-based and waterborne tem survey: Geophysics, **88**, no. 5.